



# The Solar Disk at High Energies

Miguel Gutiérrez, Manuel Masip , and Sergio Muñoz

CAFPE and Departamento de Física Teórica y del Cosmos, Universidad de Granada, E-18071 Granada, Spain

Received 2022 June 14; revised 2022 October 21; accepted 2022 November 2; published 2022 December 14

## Abstract

High energy cosmic rays *illuminate* the Sun and produce an image that could be observed in up to five different channels: a cosmic-ray shadow (whose energy dependence has been studied by HAWC); a gamma-ray flux (observed at  $E \leq 200$  GeV by Fermi-LAT); a muon shadow (detected by ANTARES and IceCube); a neutron flux (undetected, as there are no hadronic calorimeters in space); a flux of high energy neutrinos. Since these signals are correlated, the ones already observed can be used to reduce the uncertainty in the still undetected ones. Here we define a simple setup that uses the Fermi-LAT and HAWC observations to imply very definite fluxes of neutrons and neutrinos from the solar disk. In particular, we provide a fit of the neutrino flux at 10 GeV–10 TeV that includes its dependence on the zenith angle and on the period of the solar cycle. This flux represents a *neutrino floor* in indirect dark matter searches. We show that in some benchmark models the current bounds on the dark matter–nucleon cross section push the solar signal below this neutrino floor.

*Unified Astronomy Thesaurus concepts:* [Cosmic rays \(329\)](#); [Gamma-rays \(637\)](#); [Neutrino telescopes \(1105\)](#); [Solar physics \(1476\)](#)

## 1. Introduction

The surface of the Sun is at a temperature  $T \approx 0.5$  eV, while its core is burning hydrogen at  $T \approx 1$  keV. Nuclear reactions there produce neutrinos that reach the Earth unscattered with energies of up to 10 MeV. In addition, solar flares are able to accelerate nuclei and electrons up to a couple of GeV. The Sun, however, can also be observed at energies above GeV. The emission in these other channels is indirect: instead of particles accelerated by the Sun, it appears when high energy cosmic rays (CRs) *illuminate* its surface. In particular, EGRET (Orlando & Strong 2008) and Fermi-LAT (Abdo et al. 2011; see also Linden et al. 2018, 2022) have observed a sustained flux of gamma rays coming from the solar disk that extend up to 200 GeV. The signal, stronger during a solar minimum and interpreted as the albedo flux produced by CRs showering in the Sun’s surface, is 10 times above the diffuse gamma-ray background and six times larger than a 1991 estimate by Seckel, Stanev, and Gaisser (Seckel et al. 1991). Obviously, the same mechanism should produce as well as neutrinos (Édsjo et al. 2017; Ng et al. 2017; Argüelles et al. 2017; Masip 2018) and neutrons, which are also neutral and thus able to reach the Earth revealing their source.

Although the solar emission of high energy particles induced by CRs was already discussed 30 yr ago, a precise calculation is in principle plagued by the uncertainties introduced by the solar magnetism (Mazziotta et al. 2020). Here we propose a complete and consistent framework that avoids these difficulties by using the data and implies a clear correlation among the different signals that may be accessible at several astroparticle observatories. If observed, they would provide a multi-messenger picture of the Sun complementary to the one obtained with light, keV–MeV neutrinos, or solar probes.

## 2. Absorption of Cosmic Rays

If we point with a detector of CRs to the Sun, we will observe a shadow: the CR shadow of the Sun (Amenomori et al. 2013). Suppose there were no solar magnetisms, so that CRs follow straight lines. Then the trajectories aiming to Earth but absorbed by the Sun would define a black disk of radius  $r = 0.26$ : the angular size of the Sun as seen from Earth. Indeed, this is what we will see at very high energies, when the deflection of CRs by the solar magnetic field is negligible, but not at lower energies. CRs of energy below 100 TeV are very affected by a magnetic field that, unfortunately, is very involved. First of all, it has a radial component (open lines that define the Parker interplanetary field; Tautz et al. 2011) that grows like  $1/R^2$  as we approach the surface. This gradient in the field may induce a magnetic mirror effect: CRs approaching the Sun tend to bounce back. In addition, the solar wind induces convection, i.e., CRs are propagating in a plasma that moves away from the Sun and makes it more difficult to reach the surface. Finally, closer to the Sun, the magnetic turbulence increases and there appears new types of field lines that start and end on the solar surface. Hopefully, we can understand the absorption rate of CRs by the Sun with no need to solve these details, just by using the data on its CR shadow together with Liouville’s theorem.

The data is provided by HAWC (Enriquez-Rivera & Lara 2015), which has studied the energy dependence of the CR shadow during a solar maximum. The shadow appears at 2 TeV; it is not a black disk of  $r = 0.26$  but a deficit that extends into a larger angular region. By integrating it we find that at 2 TeV it accounts for a 6% of a black disk, the deficit grows to 27% at 8 TeV, and at 50 TeV it becomes a 100% deficit, i.e., a complete solar black disk diluted in a  $2^\circ$  circle.

HAWC data suggest a simple interpretation based on Liouville’s theorem. The theorem implies that when the isotropic CR flux crosses the solar magnetic field, it stays isotropic, and the only possible effect of the Sun is to interrupt some of the trajectories that were aiming to Earth. As we illustrate in Figure 1, the solar magnetic field deflects some of



Original content from this work may be used under the terms of the [Creative Commons Attribution 4.0 licence](#). Any further distribution of this work must maintain attribution to the author(s) and the title of the work, journal citation and DOI.

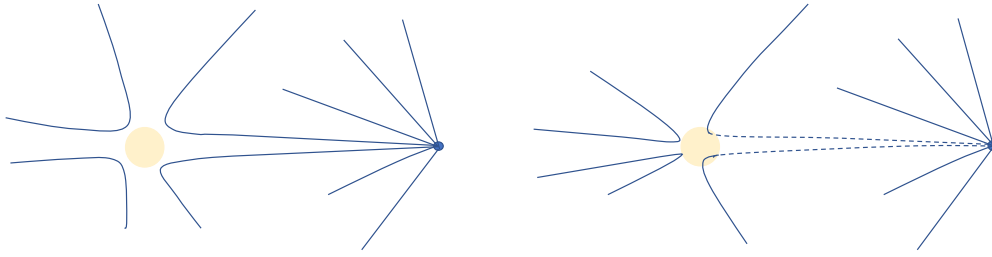


**Figure 1.** Schematic CR trajectories in the vicinity of the Sun. The solar magnetism does not create anisotropies in the flux reaching the Earth, but the average depth of solar matter crossed by CRs grows with the energy, increasing their probability to be absorbed and thus the integrated CR shadow observed by HAWC.

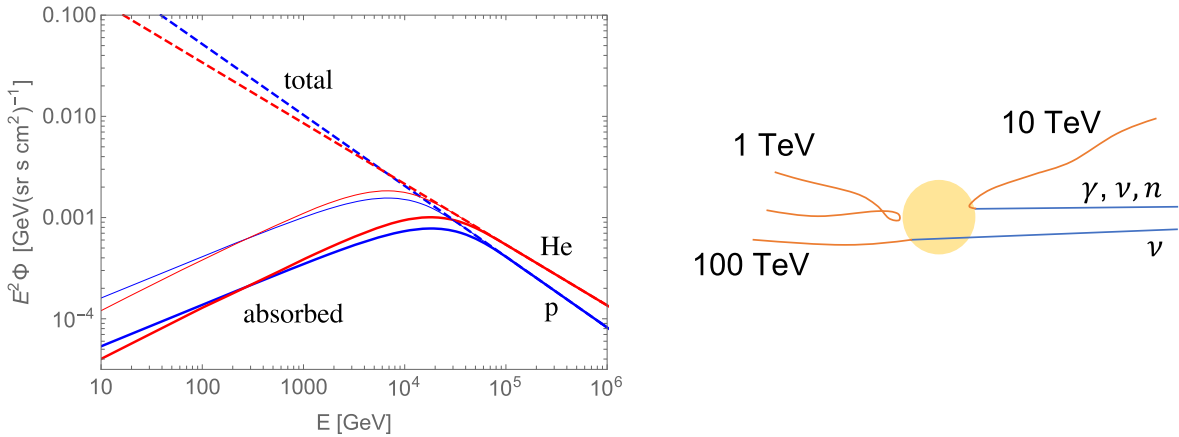


**Figure 2.** Absorbed proton and He fluxes during a solar maximum (thick) and a solar minimum (thin). On the right, typical CR trajectories at different energies.

the trajectories directed to Earth, but other trajectories will now reach us and the net effect should be zero: an isotropic flux crossing a static magnetic lens, including a mirror, will stay isotropic<sup>1</sup>, and the only possible effect is to create a shadow. At low energies HAWC sees no shadow, meaning that a negligible fraction of the CR flux reaches the solar surface. At higher energies, however, CRs that were supposed to reach the detector hit before the Sun and are absorbed (Figure 1, right). Therefore, studying the shadow we may deduce the average depth of solar matter crossed by CRs of different energy on their way to Earth.

If a CR proton crosses an average depth of  $\Delta X_H(E)$  the probability to be absorbed is

$$p_{\text{abs}}^H = 1 - \exp\left(-\frac{\Delta X_H}{\lambda_{\text{int}}^H}\right). \quad (1)$$

To explain the data we will assume

$$\frac{\Delta X_H}{\lambda_{\text{int}}^H} = b_H E^{1.11}, \quad (2)$$

with  $E$  in GeV and a time-dependent parameter  $b_H$  that oscillates between  $1.6 \times 10^{-5}$  during a solar maximum and  $4.8 \times 10^{-5}$  during a minimum. Since the trajectory of a CR only depends on its rigidity, He nuclei of twice the energy cross

<sup>1</sup> The theorem states that the density of CR trajectories in 6D phase space is constant along any trajectory. If all directions are equally populated and the solar magnetic field does not change  $|p|$ , this implies that the differential flux (number of CRs per unit area and solid angle) will be constant along the trajectory. An analogous situation may be found in optics. If we place a lens in a room with just isotropic (diffuse) light, the lens will not appear brighter nor produce any changes in the intensity of the light that we see: the isotropic flux stays isotropic after crossing the lens.

the same average depth and

$$b_{\text{He}} = \frac{b_H}{2^{1.11}} \frac{\sigma_{\text{He}}(E)}{\sigma_H(E/2)}. \quad (3)$$

Equation (2) is then the first and key hypothesis in our framework. It implies the absorption of CR primaries given in Figure 2, left, where we have considered a CR flux with only proton and He nuclei and slightly different spectral indexes ( $-2.7$  and  $-2.6$ , respectively).

This absorption determines whether the CR shadow that we see at different energies is partial or complete. At low energies CRs are unable to reach the solar surface: the depth of solar matter that they cross is small, they are not absorbed and we see no shadow. At high energies CRs that were supposed to reach the Earth find a large column density of solar matter and are absorbed; thus we see a complete shadow. Our choice for the 1.11 spectral index and for the value of  $b_H$  during an active phase of the Sun is based only on HAWC observations (we discuss our fit to that data in Section 4), whereas the value of  $b_H$  during a quiet Sun provides our best fit for the Fermi-LAT data (described in Section 3).

Next we need to model the showering of these absorbed fluxes. A numerical simulation shows that at TeV energies only trajectories that are very aligned with the open field lines are able to reach the Sun's surface. Once there, CRs will shower; some of the secondaries will be emitted inwards, toward the Sun, but others will be emitted outwards and may eventually reach the Earth. The probability that a secondary particle contributes to the solar albedo flux will depend on how deep it is produced and in which direction it is emitted.

We assume that secondaries produced by a parent of energy  $E$  above some critical energy  $E_c$  that varies between 6 and 3 TeV for an active or quiet Sun, respectively, will most likely be

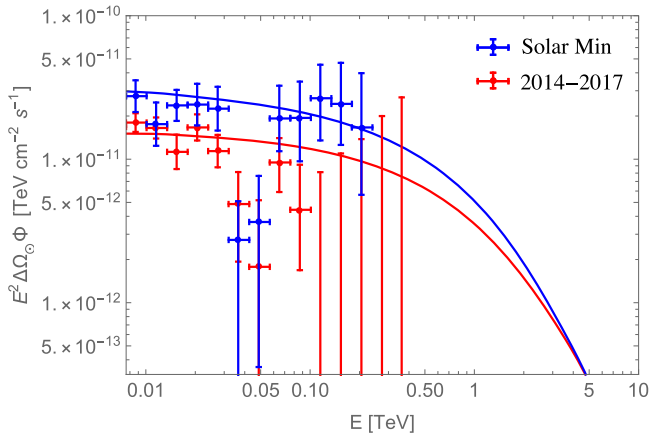


**Figure 3.** Gamma-ray flux from the solar disk (data from Fermi-LAT; Linden et al. 2018).

emitted toward the Sun, whereas lower energy primaries will exit in a random direction:<sup>2</sup>

$$p_{\text{out}} = \frac{1}{2} e^{-(E/E_c)^2}. \quad (4)$$

Accordingly, we also assume that charged particles of energy below  $E_c$  are unable to keep penetrating the Sun: they are trapped by closed magnetic lines at the depth where they are produced and shower horizontally. Equation (4) is then the second basic hypothesis in our framework; the value of  $E_c$  has been chosen to reproduce the drop in the gamma-ray flux observed by Fermi-LAT at energies above 200 GeV (see also Albert et al. 2018).

Under the two assumptions expressed in Equations (2) and (4), we use cascade equations (Gaisser 1990) to find the final albedo flux of neutral particles (see the complete equations in Masip 2018; G3mez et al. 2020). The key difference with the usual showers in Earth’s atmosphere is due to the thin environment where these solar showers develop: below the optical surface of the Sun, it takes 1500 km to cross just  $100 \text{ g cm}^{-2}$ . As a consequence, TeV pions and even muons decay before they lose energy, defining photon and neutrino fluxes well above the atmospheric ones. For neutrinos, to the albedo flux we must add the neutrinos produced in the opposite side of the Sun (Argu3lles et al. 2017; Edsjo et al. 2017; Ng et al. 2017). Our results for the signal in the different channels are in the following.

### 3. Gamma Rays

In Figure 3 we plot the flux of gamma rays at  $E > 10 \text{ GeV}$  in our setup together with the Fermi-LAT data. The normalization of the blue line in that figure is controlled by the value of  $b_H$  in Equation (2) chosen for a quiet Sun, which also implies the absorption rate of CRs for a quiet Sun given in Figure 2, left (thin lines). The spectrum of gamma rays exhibits two main features. At low energies it is reduced because primary CRs do not reach the Sun; notice that during a solar minimum it is easier for CRs to reach the solar surface, implying a more complete shadow and a larger gamma-ray flux. At higher energies the gamma flux is reduced as well, but because of a different reason: all CRs reach the surface in their way to Earth

<sup>2</sup> Notice that  $E_c$  is a factor of 2 larger when the parent particle is a He nucleus.

through the solar magnetic field and shower there, but most photons are emitted toward the Sun. Although the setup does not provide a reason for the possible *dip* at 40 GeV (Tang et al. 2018), the 400–800 photons per squared meter and year that we obtain seem an acceptable fit of the data.

### 4. Neutrons, CR Shadow, and Muon Shadow

Our analysis implies an average of 240 neutrons of energy above 10 GeV reaching the Earth from the solar disk per squared meter and year, with the flux during a solar minimum a factor of 2 larger than during an active phase of the Sun. Most of these neutrons come from the spallation of He nuclei (see Figure 4, left), resulting in a very characteristic spectrum that peaks at 1–5 TeV. The flux is interesting because neutrons are unstable: they can reach us from the Sun, but not from outside the solar system. In a satellite experiment the background to this solar flux would be the albedo flux from CRs entering the atmosphere, which seems easily avoidable. Unfortunately, space observatories do not carry hadronic calorimeters and are thus unable to detect neutrons.

The solar neutron flux, in turn, has another effect as it enters the atmosphere: it *reduces* the CR shadow of the Sun measured by HAWC. In Figure 4, right we give the total shadow (fraction of CRs absorbed by the Sun minus the relative number of neutrons reaching the Earth) predicted by our framework together with HAWC data, which were obtained near a solar maximum.

In addition to the CR shadow and the gamma and neutron signals, another interesting channel observable at neutrino telescopes (already detected at ANTARES, Albert et al. 2020 and IceCube, Aartsen et al. 2021) would be the muon shadow of the Sun when it is above the horizon: down-going muons entering the telescope from the direction of the solar disk. These muons are produced when both the partial shadow of the Sun and the solar neutrons shower in the atmosphere. In Figure 5 we plot our results as a function of the muon energy (left) or the slant depth at the point of entry in the telescope (right).

The plot for the muon shadow at different slant depths is especially revealing. It compares the number of tracks from the solar disk (smeared into a larger angular region) and from a *fake* Sun at the same zenith inclination. To observe it in a telescope, one should bin the slant depth of the muon tracks entering the detector and then determine the deficit (integrated to the whole angular region) relative to the fake Sun, finding the fraction of a black disk of  $r_\odot = 0^\circ 26'$  that it represents. In IceCube (Achterberg et al. 2006) the Sun is always very low in the horizon, implying that most muon tracks arrive after crossing a large slant depth, are very energetic and thus give a more complete muon shadow of the Sun than, for example, KM3NeT (Adrian-Martinez et al. 2016). This second telescope will access the Sun more vertically and thus from smaller slant depths (down to 3500 mwe), which could establish a more clear energy dependence of this muon shadow. In any case, the data published by IceCube (Aartsen et al. 2021) exhibits two qualitative features that are fully consistent with our framework: a more complete shadow at higher energies<sup>3</sup>; and a more complete shadow during a quiet Sun.

<sup>3</sup> Notice that they give the results in terms of the primary CR energy, which is typically 10 times larger than the energy of the muons in our Figure 5.

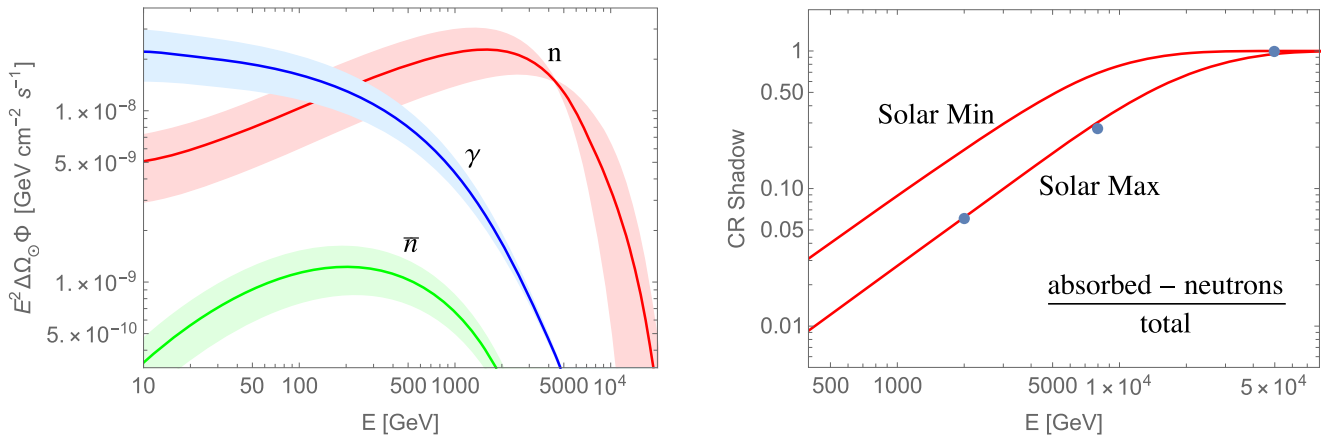


**Figure 4.** Gamma and neutron fluxes (left) and integrated CR shadow from the solar disk (right); the dots correspond to the HAWC observation (Enriquez-Rivera & Lara 2015).

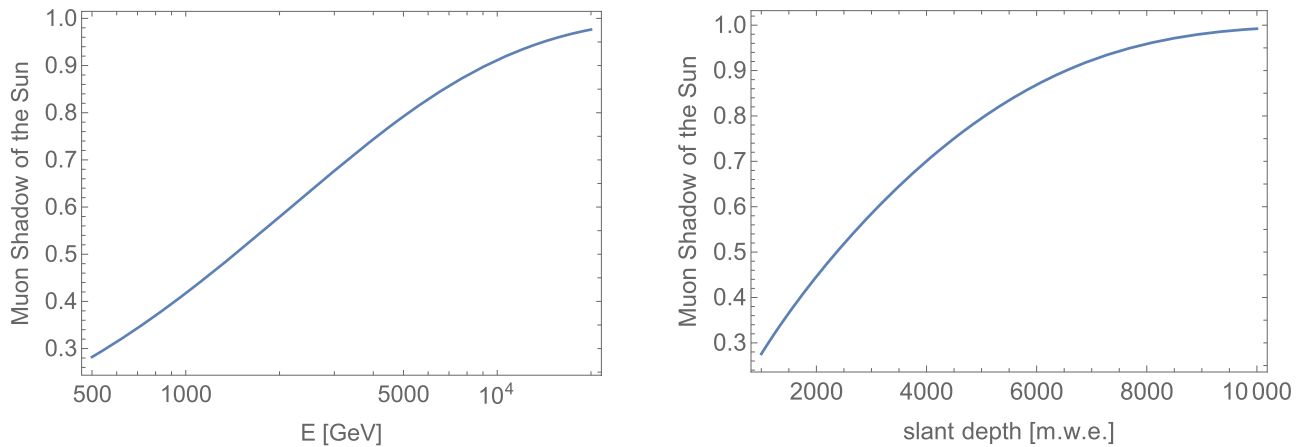


**Figure 5.** Muon shadow of the Sun at different muon energies (left) or slant depths (right).

### 5. Neutrinos from the Solar Disk

The neutrino flux reaching a telescope includes three different components:

1. Neutrinos produced in Earth's atmosphere by the partial CR shadow of the Sun. At CR energies above 50 TeV the shadow is complete and this component vanishes, but at lower energies the shadow disappears and this component should coincide with the atmospheric  $\nu$  flux.
2. Neutrinos produced in the atmosphere by the solar neutrons reaching the Earth.
3. The neutrinos produced in the solar surface, both the albedo flux and the flux from the opposite side that reaches the Earth after crossing the Sun.

The first two components are absent in all previous analyses. As for the third one, several groups (Argüelles et al. 2017; Edsjo et al. 2017; Ng et al. 2017) have obtained the neutrino flux produced by CRs showering in the opposite side of the Sun unaffected by the solar magnetic field (see Figure 2). Their results are larger than ours at energies  $E < 500$  GeV (in our setup low energy CRs do not reach the Sun), 30% smaller at  $E \approx 1$  TeV (our albedo flux is not partially absorbed by the Sun on its way to Earth), and similar at  $E > 10$  TeV (at high energies neutrinos are produced always inwards). In Figure 6, left, we plot the flux of neutrinos produced in the solar surface together with the albedo flux of gammas and neutrons for

comparison. We see that at low energy neutrinos more than *double* the number of gammas, whereas at  $E > 5$  TeV all albedo fluxes vanish but we still get the neutrinos produced in the opposite side of the Sun.

In Figure 6, right, we plot the three neutrino components when the Sun is  $45^\circ$  below the horizon (notice that the fluxes produced by the partial shadow and by the solar neutrons depend on the zenith angle), together with the atmospheric background. The bands express the variation during a solar cycle; the solar and neutron components are larger during a quiet Sun, whereas the  $\nu$  component from the partial shadow is larger during a solar maximum. The variation in the total neutrino flux during the 11 yr cycle (the blue band in the plot) tends to cancel and is below the 25% at 200 GeV.

We see that the total neutrino flux from the solar disk is well above the atmospheric background at  $E > 100$  GeV. In Figure 7, left, we compare the two fluxes when the Sun is  $45^\circ$  or  $10^\circ$  below the horizon; the second inclination is the typical one for the Sun at IceCube. We see that the signal changes little with the zenith angle, whereas the background is significantly larger when the Sun is near the horizon. In the Appendix we provide an analytical fit to these components in the neutrino flux, giving the dependence on  $\theta_z$  and on the period in the solar cycle. In Figure 7, right, we plot the signal to background ratio. Since the neutrinos produced in the Sun reach the Earth with the same frequency for the three flavors,

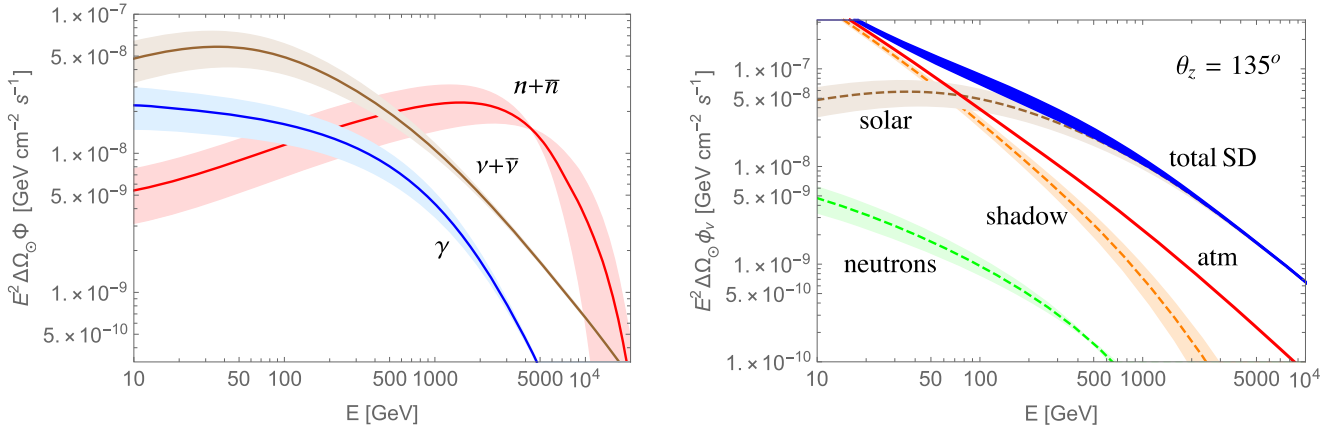


**Figure 6.** Solar neutrino flux (left) and components defining the neutrino flux observed in a telescope from the solar disk at  $\theta_z = 135^\circ$  and atmospheric background at the same zenith inclination (right).

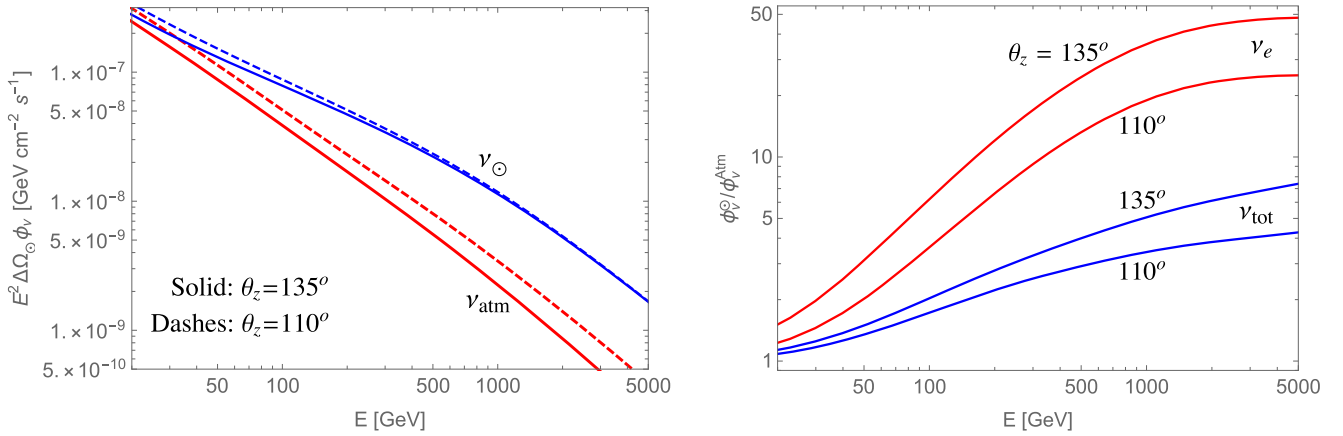


**Figure 7.** Total neutrino flux from the solar disk versus atmospheric background for the Sun in two different zenith inclinations (left). Signal to background ratio for  $\nu_e$  and for the sum of all flavors (right).

the ratio is obviously much larger for the  $\nu_e$  than the  $\nu_\mu$  flavor, and it grows with the energy and with the zenith inclination.

## 6. Solar Neutrino Floor in Indirect Searches

The annihilation of dark matter (DM) particles  $\chi$  captured by the Sun may produce a  $\nu$  flux that, to be detectable, must be above the solar flux just obtained. Here we would like to show how to estimate the minimum DM–nucleon collision cross section that would be accessible in indirect searches.

Let us assume a DM annihilation cross section large enough to establish a stationary regime where the capture rate is equal to twice the annihilation rate (Jungman et al. 1996). For illustration, we will consider three possible annihilation channels:  $\chi\bar{\chi} \rightarrow \tau^+\tau^-$ ,  $\chi\bar{\chi} \rightarrow b\bar{b}$ , and  $\chi\bar{\chi} \rightarrow W^+W^-$ . We parameterize the spin-independent (SI) and spin-dependent (SD) DM–nucleon cross sections (Fitzpatrick et al. 2013)

$$\sigma_{\chi N}^{\text{SI}} = \frac{\mu_N^2}{\pi} (c_1^N)^2; \quad \sigma_{\chi N}^{\text{SD}} = \frac{3\mu_N^2}{16\pi} (c_4^N)^2, \quad (5)$$

with  $N=p, n$ , and  $\mu_N = m_N m_\chi / (m_N + m_\chi)$ . To deduce the elastic cross section with the six most abundant solar nuclei (H, He, N, O, Ne, Fe) we use the nuclear response functions in Catena & Schwabe (2015). As it is customary in direct searches, we will take equal proton and neutron SI couplings

( $c_1^n = c_1^p$ ) and will only consider the SD coupling of the proton ( $c_4^n = 0$ ).

In our estimate for the capture rate we use the AGSS09 solar model (Asplund et al. 2009) and the SHM<sup>++</sup> velocity distribution of the galactic DM (Evans et al. 2019). We include the thermal velocity for the solar nuclei, which gives a sizeable contribution (6% increase) in the captures through SD interactions (dominated by hydrogen). We obtain the neutrino yields after the propagation from the Sun to the Earth for each annihilation channel with DarkSUSY (Bringmann et al. 2018).

To illustrate the reach of DM searches at  $\nu$  telescopes, let us fix  $m_\chi = 500$  GeV. For a DM particle that is captured through SI collisions and annihilates into  $\tau^+\tau^-$ , a neutrino flux above the solar background established in the previous section requires  $\sigma_{\chi N}^{\text{SI}} > 9.7 \times 10^{-46}$  cm<sup>2</sup>. If the annihilation channels are  $W^+W^-$  and  $b\bar{b}$  then the elastic cross section must be  $\sigma_{\chi N}^{\text{SI}} > 3.1 \times 10^{-45}$  cm<sup>2</sup> and  $\sigma_{\chi N}^{\text{SI}} > 3.0 \times 10^{-44}$  cm<sup>2</sup>, respectively. These cross sections, however, are already excluded by direct searches at XENON1T (Aprile et al. 2018):  $\sigma_{\chi N}^{\text{SI}} < 4.4 \times 10^{-46}$  cm<sup>2</sup>. In Figure 8 we plot the neutrino fluxes at Earth for this maximum value of  $\sigma_{\chi N}^{\text{SI}}$  together with the solar background. The fluxes from DM annihilation are below the solar background in the whole energy range. If DM had only SI interactions with matter, and it had this mass and annihilation channels, indirect searches would reach the solar neutrino floor before they discover it.

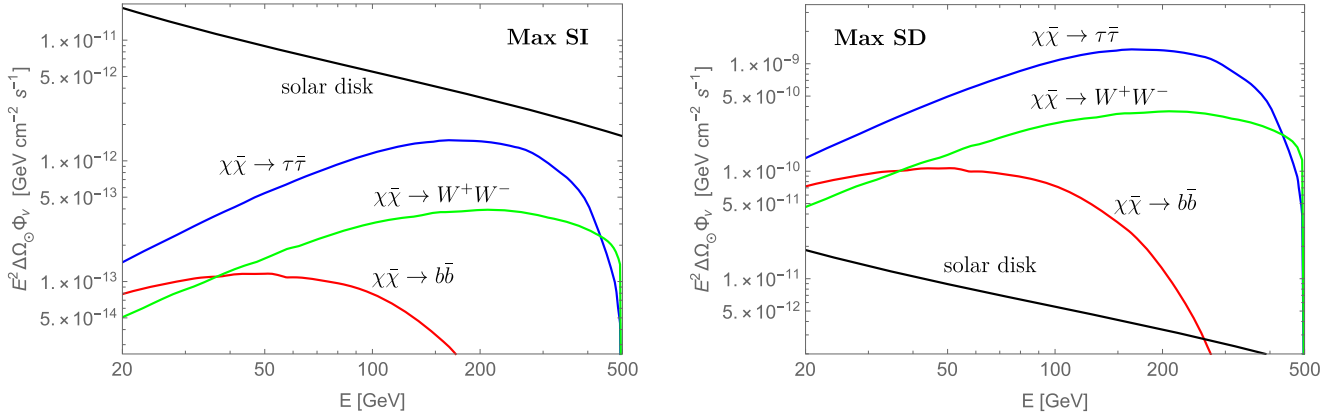


**Figure 8.** Maximum neutrino flux from DM annihilation consistent with the bounds on  $\sigma_{\chi N}^{\text{SI}}$  (left) and  $\sigma_{\chi N}^{\text{SD}}$  (right) from direct searches for the three annihilation channels that we have considered.

Indirect searches could discover DM only if it had monochromatic annihilation channels (e.g.,  $\chi\bar{\chi} \rightarrow \nu X$ ) or a large spin-dependent (SD) cross section, which is much less constrained. In particular, PICO-60 establishes that  $\sigma_{\chi p}^{\text{SD}} < 1.8 \times 10^{-40} \text{ cm}^2$  at  $m_\chi = 500 \text{ GeV}$  (Amole et al. 2019), while a DM that annihilates into  $W^+W^-$  requires just  $\sigma_{\chi p}^{\text{SD}} > 1.6 \times 10^{-42} \text{ cm}^2$  to be above the flux of solar neutrinos.

## 7. Summary and Discussion

TeV CRs induce an indirect solar emission that was discussed more than 30 yr ago and that just recently has been detected in gamma rays. Here we have used the energy dependence of the shadow of the Sun at HAWC to define a setup that implies very definite fluxes of gammas, neutrons, and neutrinos. The setup is very simple, it is based on Equation (2), which describes the average depth of solar matter crossed by protons at different energies, and in Equation (4), which estimates the probability that a secondary particle is emitted inwards or outwards depending on the energy of the parent particle. Our framework explains the peculiar spectrum of solar gammas observed at Fermi-LAT: low energy CRs do not contribute to the albedo flux as they do not reach the solar surface, whereas high energy CRs reach the Sun, but they produce gammas that are emitted mostly inwards and never reach the Earth. As we discuss in Section 4, our framework could be confirmed if HAWC completed to the full solar cycle their analysis of the shadow, or if KM3NeT and IceCube established a clear a slant-depth dependence in the muon shadow of the Sun. Of course, new channels and a higher precision in the channels already observed would also test it. The framework may also have implications on the data (at much lower energies) provided by the IS $\odot$ IS experiment (Christian et al. 2021; Malandraki et al. 2022) at the Parker Solar Probe. It seems clear that the combined analysis of the five different signals that we propose would draw a more complete picture of the solar magnetism and of the propagation of CRs near the surface.

The neutrino fluxes from the solar disk are especially interesting (Ardid et al. 2018; Aartsen et al. 2021; Villarreal et al. 2021; Albert et al. 2022), as there is currently an important experimental effort devoted to indirect DM searches (see Berger et al. 2022 and references therein). We show that the neutrino fluxes reaching a telescope include three components: (i) the solar emission from both sides of the

Sun, (ii) neutrinos produced when the partial CR shadow of the Sun enters the atmosphere, and (iii) neutrinos produced also in the atmosphere by the albedo flux of solar neutrons. The two last contributions have not been discussed in previous literature. In the Appendix we provide fits for these components, giving their explicit dependence on the zenith angle and the period of the 11 yr solar cycle. The uncertainty in the fluxes is mainly correlated with the uncertainty in HAWC data on the CR shadow of the Sun, and we estimate it at the 30% level. One should keep in mind, however, that the solar magnetism is not stable at all; if we quantify the activity in terms of the number sunspots, 1 yr periods of the solar activity present fluctuations of the order of 50%, which could be a fair estimate of the total uncertainty in the parameters defining the model and in the annual fluxes that we obtain.

The neutrinos produced in the solar surface define a floor in DM searches. In particular, we find that the maximum SI elastic cross section consistent with current bounds from XENON1T implies a flux of neutrinos from DM annihilations into  $\tau^+\tau^-$ ,  $b\bar{b}$ , or  $W^+W^-$  already below this floor. Therefore, a precise characterization of the  $\nu$  fluxes from the solar disk induced by CRs is essential both to decide the optimal detection strategy and to establish the reach of indirect DM searches at each neutrino telescope.

This work was partially supported by the Spanish Ministry of Science, Innovation and Universities (PID2019-107844GB-C21/AEI/10.13039/501100011033) and by the Junta de Andalucía (FQM 101, P18-FR-5057).

## Appendix Fit to the Neutrino Fluxes

Here we provide approximate fits for the atmospheric and solar fluxes integrated over the angular region ( $\Delta\Omega_\odot$ ) occupied by the Sun. In these expressions  $E$  is in GeV and  $t$  in years ( $t=0$  at the solar minimum), whereas  $\Delta\Omega_\odot \Phi_{\nu_\mu}^{\text{atm}}$  is given in  $\text{GeV cm}^{-2} \text{ s}^{-1}$ . The angle  $\theta^*(\theta_z)$  is defined in Lipari (1993) and Gutiérrez et al. (2022):

$$\tan \theta^* = \frac{R_\oplus \sin \theta_z}{\sqrt{R_\oplus^2 \cos^2 \theta_z + (2R_\oplus + h)h}}. \quad (\text{A1})$$

For the atmospheric flux we have

$$\Delta\Omega_{\odot} \Phi_{\nu_{\mu}}^{\text{atm}}(E, \theta) = 0.068 \\ \times E^{-2.97-0.0108 \log E - 0.00141 \log^2 E} F_1^{\text{atm}}(E, \theta); \quad (\text{A2})$$

$$\Delta\Omega_{\odot} \Phi_{\nu_e}^{\text{atm}}(E, \theta) = 0.030 \\ \times E^{-3.30-0.0364 \log^{1.35} E + 0.0103 \log^{1.85} E} F_2^{\text{atm}}(E, \theta) \quad (\text{A3})$$

with

$$F_1^{\text{atm}}(E, \theta) = \frac{\left(\frac{176}{E}\right)^{0.6} + \cos[\theta^*(\frac{\pi}{4})]}{\left(\frac{176}{E}\right)^{0.6} + \cos[\theta^*(\theta_z)]}; \\ F_2^{\text{atm}}(E, \theta) = \frac{\left(\frac{7.5 \times 10^{-4}}{E}\right)^{0.21} + \cos[\theta^*(\frac{\pi}{4})]}{\left(\frac{7.5 \times 10^{-4}}{E}\right)^{0.21} + \cos[\theta^*(\theta_z)]}. \quad (\text{A4})$$

For the atmospheric neutrinos from both the CR shadow of the Sun and solar neutrons

$$\Delta\Omega_{\odot} \Phi_{\nu_{\mu}}^{\text{shad+n}}(E, \theta, t) = 0.0670 E G_1^{\text{atm}}(E, t) F_2^{\text{atm}}(E, \theta); \quad (\text{A5})$$

$$\Delta\Omega_{\odot} \Phi_{\nu_e}^{\text{shad+n}}(E, \theta, t) = 0.0212 E G_2^{\text{shad+n}}(E, t) F_2^{\text{atm}}(E, \theta) \quad (\text{A6})$$

with

$$G_1^{\text{shad+n}}(E, t) = -2.98 - 0.017 \log E + 0.012 \cos \frac{2\pi t}{11} \log^2 \\ \times E - 3.3 \times 10^{-4} \log^3 E - 4.1 \times 10^{-6} \log^5 E; \quad (\text{A7})$$

$$G_2^{\text{shad+n}}(E, t) = -3.1 - 0.061 \log E - \cos \frac{2\pi t}{11} \\ (0.00305 \log E + 2.1 \times 10^{-6} \log^5 E) - 5.3 \times 10^{-7} \log^6 E. \quad (\text{A8})$$

Finally, the neutrinos produced in the Sun come in the three flavors with the same frequency and

$$\Delta\Omega_{\odot} \Phi_{\nu_i}^{\odot}(E, t) = \left( 0.917 \times 10^{-4} - \frac{0.037 \sin^2 \frac{\pi t}{11}}{900 + E} \right) \\ \times E^{-1.20-0.1 \log E - 0.0042 \log^2 E + 1.6 \times 10^{-5} \log^4 E}. \quad (\text{A9})$$

## ORCID iDs

Manuel Masip  <https://orcid.org/0000-0002-7750-2514>

## References

- Aartsen, M. G., Ackermann, M., Adams, J., et al. 2021, *JCAP*, **2**, 025  
Aartsen, M. G., Abbasi, R., Ackermann, M., et al. 2021, *PhRvD*, **103**, 042005  
Abdo, A. A., Ackermann, M., Ajello, M., et al. 2011, *ApJ*, **734**, 116  
Achterberg, A., Ackermann, M., Adams, J., et al. 2006, *Aph*, **26**, 155  
Adrian-Martinez, S., Ageron, M., Aharonian, F., et al. 2016, *JPhG*, **43**, 084001  
Albert, A., Alfaro, R., Alvarez, C., et al. 2018, *PhRvD*, **98**, 123011  
Albert, A., Alves, S., André, M., et al. 2022, *JCAP*, **06**, 018  
Albert, A., André, M., Anghinolfi, M., et al. 2020, *PhRvD*, **102**, 122007  
Amenomori, M., Bi, X.J., Chen, D., et al. 2013, *PhRvL*, **111**, 011101  
Amole, C., Ardid, M., Arnquist, I.J., et al. 2019, *PhRvD*, **100**, 022001  
Aprile, E., Aalbers, J., Agostini, F., et al. 2018, *PhRvL*, **121**, 111302  
Ardid, M., Felis, I., Lotze, M., et al. 2018, *ICRC (Busan)*, **35**, 907  
Argüelles, C. A., de Wasseige, G., Fedynitch, A., & Jones, B. J. P. 2017, *JCAP*, **07**, 024  
Asplund, M., Grevesse, N., Sauval, A. J., & Scott, P. 2009, *ARA&A*, **47**, 481  
Berger, J., Brailsford, D., Choi, K., et al. 2022, arXiv:2207.02882  
Bringmann, T., Edsjö, J., Gondolo, P., Ullio, P., & Bergström, L. 2018, *JCAP*, **07**, 033  
Catena, R., & Schwabe, B. 2015, *JCAP*, **04**, 042  
Christian, E., Cohen, C., Cummings, A.C., et al. 2021, *ICRC (Berlin)*, **37**, 1306  
Edsjo, J., Elevant, J., Enberg, R., & Niblaeus, C. 2017, *JCAP*, **06**, 033  
Enriquez-Rivera, O., & Lara, A. 2015, *ICRC (The Hague)*, **34**, 99  
Evans, N. W., O'Hare, C. A. J., & McCabe, C. 2019, *PhRvD*, **99**, 023012  
Fitzpatrick, A. L., Haxton, W., Katz, E., Lubbers, N., & Xu, Y. 2013, *JCAP*, **02**, 004  
Gaisser, T. K. 1990, *Cosmic Rays and Particle Physics* (Cambridge: Cambridge Univ. Press)  
Gámez, C., Gutiérrez, M., Martínez, J. S., & Masip, M. 2020, *JCAP*, **01**, 057  
Gutiérrez, M., Hernandez-Tome, G., Illana, J. I., & Masip, M. 2022, *Aph*, **134**, 102646  
Jungman, G., Kamionkowski, M., & Griest, K. 1996, *PhR*, **267**, 195  
Linden, T., Beacom, J. F., Peter, A. H. G., et al. 2022, *PhRvD*, **105**, 063013  
Linden, T., Zhou, B., Beacom, J. F., et al. 2018, *PhRvL*, **121**, 131103  
Lipari, P. 1993, *Aph*, **1**, 195  
Malandraki, O. E., McComas, D. J., Rodriguez-Pacheco, J., et al. 2022, *ICRC (Berlin)*, **395**, 040  
Masip, M. 2018, *Aph*, **97**, 63  
Mazziotta, M. N., De La Torre Luque, P., Di Venere, L., et al. 2020, *PhRvD*, **101**, 083011  
Ng, K. C. Y., Beacom, J. F., Peter, A. H. G., & Rott, C. 2017, *PhRvD*, **96**, 103006  
Orlando, E., & Strong, A. W. 2008, *A&A*, **480**, 847  
Seckel, D., Stanev, T., & Gaisser, T. K. 1991, *ApJ*, **382**, 652  
Tang, Q.-W., Ng, K. C. Y., Linden, T., et al. 2018, *PhRvD*, **98**, 063019  
Tautz, R. C., Shalchi, A., & Dosch, A. 2011, *JGR*, **116**, A02102  
Villarreal, J., Roellinghoff, G., Lazar, J., et al. 2021, *ICRC (Berlin)*, **37**, 1174